SAND2013-10582C

Structural Efficiency Analysis of the Sandia 100 m Wind Turbine Blade

N. Buckney,* A. Pirrera† and P. M. Weaver‡
University of Bristol, Bristol, BS8 1TR, UK
D. Todd Griffith,§
Sandia National Laboratories, Albuquerque, USA

There is a trend for increasingly powerful wind turbines because as size increases, the cost of energy decreases. With this increase in size, there is more motivation for improved rotor designs. The structural efficiency of a 100 m blade is evaluated using an analysis that accounts for the shape and material of the designs. Two baseline design concepts are compared; an all-glass design, and a design with carbon spar caps. The results show that the carbon design is a more efficient structure, as expected. More importantly, the results give a greater insight as to why the design is superior. Next, the effect of altering the position of the spar caps is tested. This analysis shows that applying an offset to the spar cap position can have a beneficial effect on structural efficiency for the key load cases. Application of the methods presented in this study provide a valuable insight into why one design is successful and can be used as a quantitative evaluation at an early design stage.

I. Introduction

A. Large wind turbines

Due to the highly competitive energy market, lowering the cost of wind energy as much as is safely possible is imperative. Lighter wind turbine blades can lower the cost of the wind turbine and enable larger, more cost-effective designs. Cost reductions are partly attributed to size increases because the power generated by a wind turbine is proportional to the rotor swept area and, hence, the square of the blade length.[1] Larger wind turbines can also be more cost effective, with fewer wind turbines required to produce the equivalent power.[2] Additionally, there is a trend to increase the size of the rotors on existing turbines for application at lower wind-speed sites. In 2012, rated wind turbine power decreased, yet rotor diameters increased to an average of 93.6 m in the USA.[2]

One issue with larger wind turbine blades is that, if the blade designs are scaled up with no change in topology or materials, the blade mass increases with the cube of the length.[1] The consequence of this *square-cube relationship* between power and mass as length increases is that blade mass increases at a higher rate than the power output. The blade mass is important because lightweight designs benefit the entire wind turbine through decreased mass-induced loads. Indeed, the cost of the rotor may represent 20% of the total, but decreasing the mass can have a significant effect by reducing the material demands, and thereby, the cost of the nacelle, tower, and foundations.[3]

As wind turbines have increased in size, the structural performance has become increasingly significant. When wind turbines were smaller the design was driven by the aerodynamic performance, but now the structural response must be considered at an earlier design stage.[4] The loads due to self-weight have become increasingly influential, yet blade design has remained largely unchanged. One view is that current blade designs have reached maturity and that without major changes there will be no significant weight and cost reductions.[5] By improving the structural efficiency of the blades through new design concepts, wind turbines could be made larger and produce more energy. This would result in a reduction in the cost of wind energy.

*PhD Student, Department of Aerospace Engineering.
†Research Assistant, Department of Aerospace Engineering
‡Professor in Lightweight Structures, Department of Aerospace Engineering.
§Principal Member of the Technical Staff.

B. Structural Efficiency

In structural design, it is the material and shape which determine the efficiency. Structural efficiency can be defined as the ability to carry the design loads safely while minimizing an objective (most commonly mass).[6] Improving structural efficiency can have obvious benefits such as reducing mass and material cost.

Ashby and Weaver created a design methodology for the evaluation and selection of section shapes and materials using shape factors and material indices.[6–8] Shape factors are used to determine the efficiency of materially usage in a structure.[8] They are dimensionless parameters, depending on shape and not scale, which compare the efficiency of a shaped section to that of a simple reference section of equal area (typically, a circular cross-section). A shape factor greater than one indicates a more efficient shape than the reference section; conversely, a shape factor less than one is less efficient. Shape factors were originally developed for simple bending but have now been expanded to account for asymmetric bending. The asymmetric bending shape factors were developed as part of an earlier study, in order to assess new structural concepts for wind turbine blades.[9]

The shape factor affects the structural efficiency but it is clear that an optimal design requires selection of both shape and material. Ashby developed a method of co-selection by developing a material index that included shape, referred to as the *performance index*.[7,10] This built upon previous research which used graphical methods for selection of material and shape.[11–13]

C. Aims and objectives

As wind turbine continue to increase in size, the *square-cube relationship* between power and blade mass means that the structural efficiency becomes increasingly important. Lighter wind turbine blades can reduce the overall cost of the entire wind turbine to enable larger, more cost-effective wind turbines. The aim of this study is to evaluate the structural efficiency of a large wind turbine blade. To achieve this aim, structural efficiency investigations are performed on an large wind turbine blade design. This analysis can be used for concept evaluation and selection while improving understanding of why a design is successful. In comparison to simple beams, wind turbine blades are complex structures composed of numerous materials. To evaluate the structural efficiency, the asymmetric bending shape factors, which were introduced in the earlier study, must now be expanded to account for multiple materials in the beam section.[9] Following this, the performance index of the designs is evaluated to account for the contributions of both material and shape to the structural efficiency. Two structural efficiency investigations are performed. The first involves comparison between all-glass and carbon designs. The second study evaluates the effect of moving the position of the spar caps.

II. Structural Efficiency

A. Beams with multiple materials

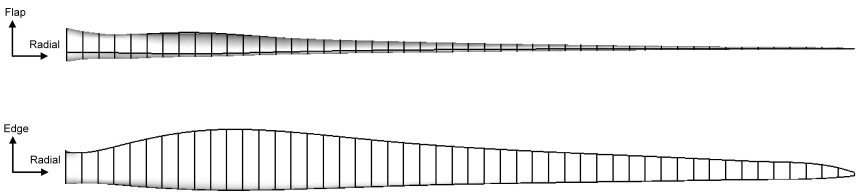

Figure 1: Wind turbine blade conventions: Side and top view.

With asymmetric bending behavior, it is vital to have a clearly defined bending convention. The radial, edgewise and flapwise directions are now defined as the x, y and z-axes using the right-hand rule (Figure 1 and 2). A positive M_y (flap moment) causes compression in the positive z-direction; positive M_z (edge moment) causes compression in the positive y-direction. In the previous study, shape factors were developed for sections composed of a single material.[9] If a section is composed of multiple materials, such as in a hybrid beam or one which uses composite materials, then the definition of the shape factors must be altered. When using multiple materials in a section it is more appropriate to work with flexural rigidity which is the

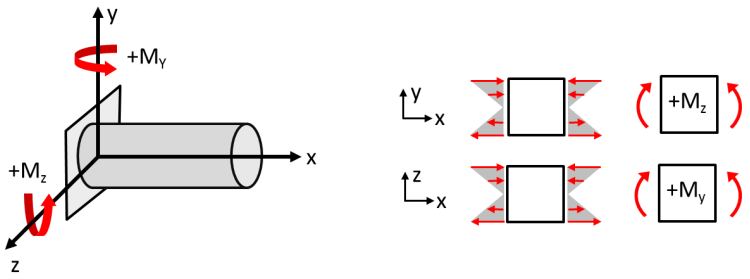

Figure 2: Bending coordinate system.

summation of EI data for each material. The flexural rigidities are

$$D_y = \sum_{\mathrm{e}=1}^{N_\mathrm{e}} E_\mathrm{e} \int_{A_\mathrm{e}} z^2 \mathrm{d}A, \tag{1a}$$

$$D_z = \sum_{\mathrm{e}=1}^{N_\mathrm{e}} E_\mathrm{e} \int_{A_\mathrm{e}} y^2 \mathrm{d}A, \tag{1b}$$

$$D_{yz} = \sum_{\mathrm{e}=1}^{N_\mathrm{e}} E_\mathrm{e} \int_{A_\mathrm{e}} yz \mathrm{d}A, \tag{1c}$$

where the summations are across N_e elemental areas. It is possible to derive new expression for the shape factors using the flexural rigidities above. Alternatively, the equivalent section properties are determined, which allows the standard formulations to be used. An average section Young's modulus is defined as

$$\overline{E} = \frac{\sum_{\mathrm{e}=1}^{N_\mathrm{e}} E_\mathrm{e} A_\mathrm{e}}{\sum_{\mathrm{e}=1}^{N_\mathrm{e}} A_\mathrm{e}}, \tag{2}$$

where the bar indicates the equivalent (or average) section properties. It is also possible to define the equivalent second moments of area as

$$\overline{I_y} = \frac{D_y}{\overline{E}}, \tag{3a}$$

$$\overline{I_z} = \frac{D_z}{\overline{E}}, \tag{3b}$$

$$\overline{I_{yz}} = \frac{D_{yz}}{\overline{E}}. \tag{3c}$$

These section properties now account for beams with multiple materials.

B. Shape Factors

The shape factors for asymmetric bending that were defined in the earlier study can now be modified by replacing the section properties with the equivalent properties.[9]

1. *Stiffness*

Stiffness is a measure of a structure's ability to resist deformation. For a structure with one degree of freedom, this is defined as the applied load divided by the resulting displacement. When evaluating the performance of a structure under bending loads, it is typical to consider its flexural rigidity which is the Young's modulus multiplied by the second moment of area.[8] The stiffness of a beam under asymmetric bending is more complex to define because of the coupled behavior which can result from a non-zero product second moment of area. The consequence of the asymmetric bending is that the maximum deflection is not always in the same direction as the applied load. For this reason, the shape factor is based upon the

deflection in a specific direction, which in this case is the z-direction (flapwise). The rationale behind this is that the flapwise deflection is the critical parameter as the blade tip must have adequate clearance from the tower. By substituting the equivalent section properties to account for the multiple materials, the shape factor for stiffness in the y-direction is defined as

$$\overline{\phi_{\mathrm{s,z}}} = \frac{4\pi M_y}{A^2}\left[\frac{\overline{I_y I_z} - \overline{I_{yz}}^2}{M_y\overline{I_z} - M_z\overline{I_{yz}}}\right], \tag{4}$$

where A is the cross-sectional area and M is the bending moment. The shape factors for single material sections assumed that the reference beam was composed of the same material. This assumption allowed the Young's modulus terms to cancel and only the effect of shape was considered. Now the shaped beam is composed of multiple materials and the reference beam is assumed to have a Young's modulus equal to $\overline{E}$. Thus, the efficiency of the shape is accounted for as well as the effect of the material distribution (which is distinct from the material index).

While it is useful to look at the shape factor for deflection in a particular direction, it is also important to consider the overall stiffness. A second stiffness shape factor is defined which is based on the magnitude of the resultant deflection, regardless of its direction. This is termed the *general stiffness* shape factor. It is calculated in the same way as the direction-specific stiffness shape factor, but now using the magnitudes of the resultant curvature as opposed to the direction specific components. It should be noted that the resultant curvature may act in a different direction to the reference beam despite being subject to the same load conditions. The general stiffness shape factor is

$$\overline{\phi_{\mathrm{s,g}}} = \frac{4\pi M_{\mathrm{res}}}{A^2}\left[\frac{\overline{I_{y'} I_{z'}} - \overline{I_{yz'}^2}}{M_{y'}\overline{I_{z'}} - M_{z'}\overline{I_{yz'}}}\right]. \tag{5}$$

where the 'res' subscript denotes the resultant and the prime indicates a rotation to the neutral axis (NA) coordinate system. The NA coordinate system is rotated from the original such that the y-axis becomes aligned with the neutral axis. Thus, the curvature around the y-axis in the NA coordinate system is the resultant curvature as the z-component is zero. This allowed the general stiffness shape factor to be expressed with one term.

2. Strain

Defining a stress shape factor for multiple materials is complicated by the dependence of the stress on the Young's modulus. While it is possible to define the shape factor using stress, a simpler expression is obtained by using strain. The strain relies on the section properties and the distance from the centroid, and not the local Young's modulus. The bending strain in the x-direction is

$$\epsilon_x = -y\kappa_z - z\kappa_y, \tag{6}$$

where κ is the curvature which is expressed using the equivalent section properties

$$\kappa_y = \frac{M_y\overline{I_z} - M_z\overline{I_{yz}}}{\overline{E}(\overline{I_y I_z} - \overline{I_{yz}}^2)} \tag{7a}$$

$$\kappa_z = \frac{M_z\overline{I_y} - M_y\overline{I_{yz}}}{\overline{E}(\overline{I_y I_z} - \overline{I_{yz}}^2)}. \tag{7b}$$

The shape factor for failure by exceeding a critical strain value is defined as

$$\phi_{\mathrm{f}} = \frac{(\epsilon_{\mathrm{x}})_0}{\epsilon_{\mathrm{x}}}. \tag{8}$$

where the subscript 0 indicates the strain of the circular reference beam. The same procedure that was used to create the stress shape factor for single material sections can be applied.[9] Substituting the strain, the shape factor for strain to failure of beams with multiple materials is

$$\overline{\phi_{\mathrm{f}}} = \frac{4\sqrt{\pi}}{A^{3/2}}\left[\frac{\overline{I_{y'} I_{z'}} - \overline{I_{yz'}^2}}{\overline{I_{z'}}z' - \overline{I_{yz'}}y'}\right], \tag{9}$$

where the prime indicates a rotation to the resultant moment (RM) coordinate system. In the RM coordinate system, the y-axis aligns with resultant moment. The shape factor expression takes the exact same form as the stress shape factor for single material sections with the difference being that the equivalent section properties are used. Although they have the same form, it is important to note that the shape factor for multiple materials is based upon strain and not stress. As the Young's modulus changes throughout the section, it is no longer appropriate to use a stress-based definition in the shape factor. The two shape factors only appear in the same form because it was possible to cancel the Young's modulus when the section was composed of a single material.

3. Shape factor examples

(a) I-beam (b) Z-beam

Figure 3: Sections to illustrate shape factor results.

Application of the shape factors is now demonstrated with two simple beam sections. An I-beam and a Z-beam are evaluated, as shown in Figure 3. These sections were chosen in order to demonstrate the effects of asymmetry ($I_1 > I_2$) on the shape factors. The principle section properties are aligned with the coordinate system for the I-beam, but not for the Z-beam.

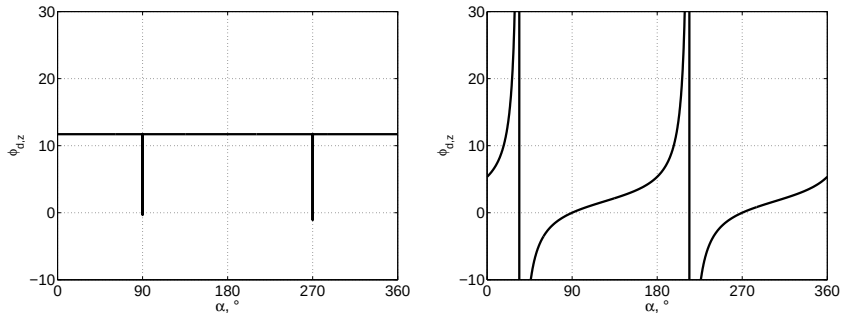

(a) I-beam (b) Z-beam

Figure 4: Shape factor for z-direction stiffness. The angular coordinate is the moment direction in degrees, α, and the radial coordinate is the shape factor, $\overline{\phi_{s,z}}$.

Figure 4 shows the shape factor for the z-direction stiffness. For the I-beam, the principal angle of the section properties is aligned with the main coordinate system, so $\overline{I_{yz}}$ is zero. This is not the case for the z-beam. The shape of the result can be further understood by replacing M_y and M_z in the shape factor with

$$M_\mathrm{y} = M_\mathrm{res} \cos\alpha, \tag{10a}$$

$$M_\mathrm{z} = M_\mathrm{res} \sin\alpha, \tag{10b}$$

where M_res is the resultant moment and α is the angle in which it is applied. These expressions are substituted into the shape factor from Equation 4, which allows the resultant moment terms to cancel

$$\overline{\phi_{\mathrm{s,z}}} = \frac{4\pi\cos\alpha}{A^2}\left[\frac{\overline{I_y I_z} - \overline{I_{yz}^2}}{\overline{I_z}\cos\alpha - \overline{I_{yz}}\sin\alpha}\right]. \tag{11}$$

The implication is that the shape factor does not depend on the magnitude of the loads, instead only on the angle of the direction in which they are applied. Alternatively, the shape factor only depends on the ratio of the two moments and not their respective magnitudes. When calculating the shape factor, it is only necessary to define α, as opposed to actual load cases with magnitudes. By taking a common factor of $\cos\alpha$, the shape factor becomes

$$\overline{\phi_{\mathrm{s,z}}} = \frac{4\pi}{A^2}\left[\frac{\overline{I_y I_z} - \overline{I_{yz}^2}}{\overline{I_z} - \overline{I_{yz}}\tan\alpha}\right]. \tag{12}$$

which explains the tan-curve shape of the z-direction stiffness shape factor. When the shape factor becomes asymptotic, this indicates that the applied load causes no deflection in the z-direction.

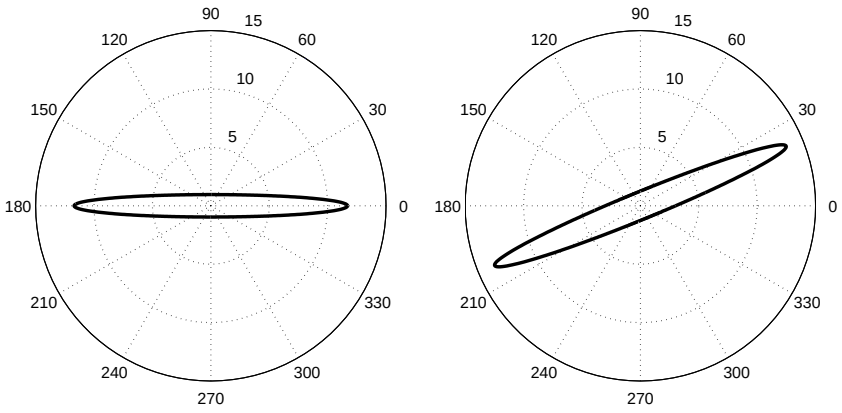

(a) I-beam (b) Z-beam

Figure 5: Shape factor for general stiffness. The angular coordinate is the moment direction in degrees, α, and the radial coordinate is the shape factor, $\overline{\phi_{s,g}}$.

The general stiffness shape factor result is shown in Figure 5. The tan-curve of the z-direction stiffness shape factor meant that Cartesian coordinates were the most appropriate way to display the results. As there is no longer a tan-curve, the result is more suited to being displayed as a polar plot. Both of the beams show a similar shape in the polar plot result, which is a narrow ellipse. The reason for this is that the beams are much stiffer in their principle directions. The obvious difference between the two beams is the rotation of the ellipse. The maximum values of the shape factor occur at the angle which corresponds to the principle angle of the second moment of area.

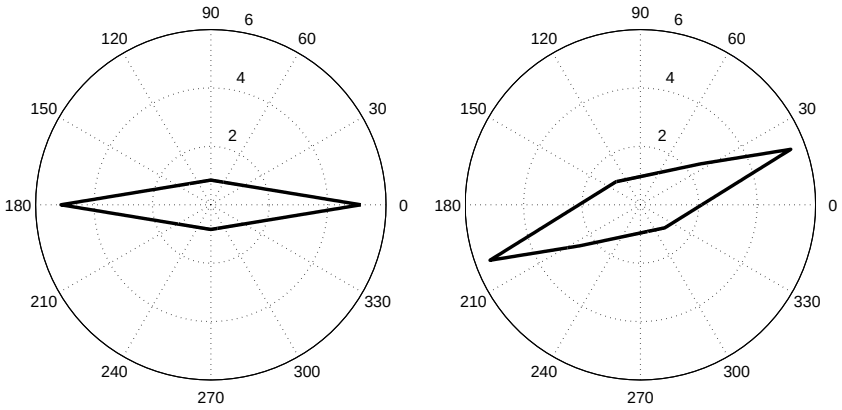

(a) I-beam (b) Z-beam

Figure 6: Shape factor for strain. The angular coordinate is the moment direction in degrees, α, and the radial coordinate is the shape factor, $\overline{\phi_f}$.

The result for the strain shape factor is shown in Figure 6. As with the general stiffness shape factor, the shape of the polar plot result is narrow and the maximum value are orientated to the principle angle of the second moment of area. A key feature of this plot is that there are sudden changes in the shape factor for small changes in angle of load direction. This effect is most prominent at the vertices of the plot. These vertices occur when the point which is the maximum distance from the neutral axis changes. For example, the point which is the maximum distance may change from the extreme left of the I-beam flange to the extreme right. This means the point at which the maximum strain occurs changes.

C. Performance Index

The effect of shape has been considered, but the material choice can also be accounted for. This involves application of the performance index to account for both material and shape. The following methods for stiffness and strain are a development from those used by Weaver and Ashby.[8]

1. Stiffness

First, we rearrange the z-direction stiffness shape factor to obtain an expression for the area

$$A = \sqrt{\frac{4\pi M_{\mathrm{y}}}{\overline{E}\kappa_{\mathrm{y}}\overline{\phi_{\mathrm{s,z}}}}}, \tag{13}$$

which is then inserted into an equation for the mass of the beam

$$m = AL\overline{\rho} = \sqrt{\frac{4\pi M_{\mathrm{y}}}{\overline{E}\kappa_{\mathrm{y}}\overline{\phi_{\mathrm{s,z}}}}}L\overline{\rho}, \tag{14}$$

where $\overline{\rho}$ is the average density of the section, defined as

$$\overline{\rho} = \frac{\sum_{\mathrm{e}=1}^{N_{\mathrm{e}}} \rho_{\mathrm{e}} A_{\mathrm{e}}}{\sum_{\mathrm{e}=1}^{N_{\mathrm{e}}} A_{\mathrm{e}}}, \tag{15}$$

The expression for the mass can then be separated into the components which are fixed parameters of the problems, such as the loading and geometry, and the parameters which can change, such as the material and shape

$$m = \sqrt{\frac{4\pi M_{\mathrm{y}}}{\kappa_{\mathrm{y}}}}L\frac{\overline{\rho}}{\sqrt{\overline{E\phi_{\mathrm{s,z}}}}}. \tag{16}$$

The objective is to minimize the mass, so the term containing the material and shape is inverted. Therefore, the performance index for z-direction stiffness is

$$M_{s,z} = \frac{\sqrt{\overline{E\phi_{\mathrm{s,z}}}}}{\overline{\rho}}. \tag{17}$$

The general stiffness performance index an be derived in the same way

$$M_{s,g} = \frac{\sqrt{\overline{E\phi_{\mathrm{s,g}}}}}{\overline{\rho}}. \tag{18}$$

2. Strain

Rearranging the equation for strain (Eq. 6) and using the RM coordinate system, we get an expression for the moment which cause failure by exceeding a critical strain value, ϵ_{x}^*

$$M_{\mathrm{res}}^* = \epsilon_{\mathrm{x}}^* \left[\frac{\overline{I_{\mathrm{y}'}I_{\mathrm{z}'}} - \overline{I_{\mathrm{yz}'}^2}}{\overline{I_{\mathrm{z}'}}z' - \overline{I_{\mathrm{yz}'}}y'} \right]. \tag{19}$$

The shape factor equation is also rearranged

$$\frac{\overline{I_{y'}I_{z'}} - \overline{I_{yz'}}^2}{\overline{I_{z'}}z' - \overline{I_{yz'}}y'} = \frac{\overline{\phi_f}A^{3/2}}{4\sqrt{\pi}}, \tag{20}$$

which can then be substituted back in the equation for the failure moment

$$M^*_{res} = \epsilon^*_x \left(\frac{\overline{\phi_f}A^{3/2}}{4\sqrt{\pi}} \right). \tag{21}$$

This is rearranged into an expression for the area

$$A = \left(\frac{4\sqrt{\pi}M^*_{res}}{\epsilon^*_x \overline{\phi_f}} \right)^{2/3}, \tag{22}$$

which is then inserted into an expression for the mass

$$m = AL\overline{\rho} = \left(\frac{4\sqrt{\pi}M^*_{res}}{\epsilon^*_x \overline{\phi_f}} \right)^{2/3} L\overline{\rho}. \tag{23}$$

The expression for the mass can then be separated into the components which are fixed parameters of the problems, such as the loading and geometry, and the parameters which can change, such as the material and shape

$$m = (4\sqrt{\pi}M^*_{res})^{2/3} L \left(\frac{\overline{\rho}}{(\epsilon^*_x \overline{\phi_f})^{2/3}} \right). \tag{24}$$

We define the performance index as the inverse of the term which includes material and shape

$$M_f = \frac{(\epsilon^*_x \overline{\phi_f})^{2/3}}{\overline{\rho}}. \tag{25}$$

III. SNL Large Rotor Development

Sandia National Laboratories (SNL) is undertaking a Large Rotor Development program. The program involves evaluating large future blade concepts for horizontal axis wind turbines. The aims are to identify challenges in the design of future large blades and promote designs that are more efficient aerodynamically, structurally, and economically.

A. 100 m Blade

SNL has developed a 100 m blade for a 13.2 MW horizontal axis wind turbine. Initially, a baseline all-glass design was developed which employed conventional materials and internal topology.[14,15] The geometry and composite layup of the all-glass blade, termed *SNL100-00*, is available online.[16] The associated turbine model is also available on the site. From this initial baseline, design improvements are made. A modified design with a carbon spar cap was created (*SNL100-01*), for which the model files are also available.[16–19] Both of these initial designs still have scope for further improvements, which may include increased use of carbon fiber, thick aerofoils, bend-twist coupling, geometric sweep, pre-bending, unique architecture, anti-buckling devices, structured core, and active control. These innovations are intended to reduce cost and weight while improving performance.[14]

The external geometry of the 100 m blade is based on a scaled up blade from the DOWEC (Dutch Offshore Wind Energy Converter) study.[20] The internal structural layout of the blade is a conventional two shear web design (a cross-section of the blade is shown in Figure 7). The design has monolithic spar caps and sandwich panels in the shear webs, leading edge panels, and trailing edge panels. Additional reinforcement has been added at the trailing edges along the blade length, as indicated in the figure. The addition of a third shear web in the aft panel was necessary to improve the resistance to buckling. The third shear web is shown in the planform of the blade (Figure 8), running from before the maximum chord to beyond the mid-span. Both blades were designed from international standards to satisfy strength, fatigue, deflection, and buckling requirements.

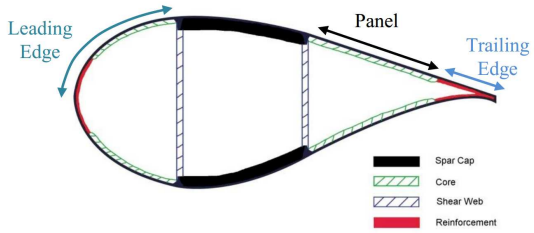

Figure 7: Cross-section of the all-glass 100 m blade (SNL00-00).[14]

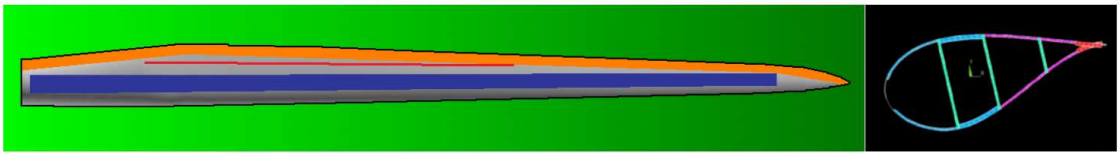

Figure 8: Planform of Sandia 100-m Baseline Blade with laminate designations (Blue: spar cap, orange: trailing edge reinforcement, red: third shear web).[14]

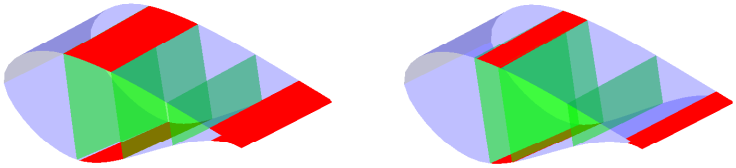

(a) Glass blade (SNL00-00) (b) Carbon blade (SNL00-01)

Figure 9: Structure of the Sandia National Laboratories 100 m blade. Spar caps and trailing edge reinforcement are shown in red, shear webs in green and panels/skin in blue.

1. *Glass blade: SNL100-00*

The *SNL00-00* blade (herein referred to as the glass blade) is designed with all-glass materials and features conventional manufacturing, including ply dropping and parasitic resin mass. The mass of the blade was 114,172 kg with a maximum tip deflection of 11.9 m. A section of the blade is shown in Figure 9a, indicating the positions of the spar caps, webs, and trailing edge reinforcement. The thickness of the root-build-up, spar cap, and trailing edge reinforcement along the blade length are given in Figure 10a. More details of the blade design are provided in the design scorecard for the blade.[21] The design scorecard has been created by SNL as a format that allows researchers to compare different blade designs.[22]

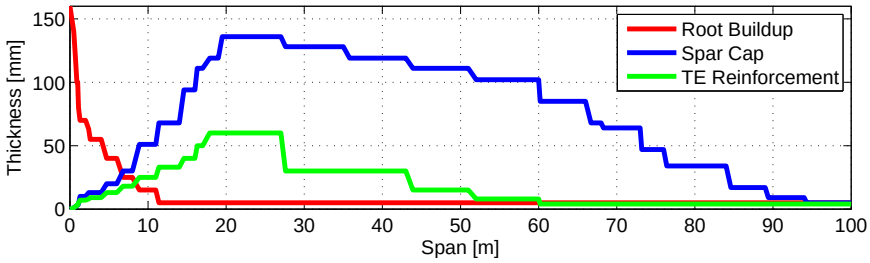

(a) Glass

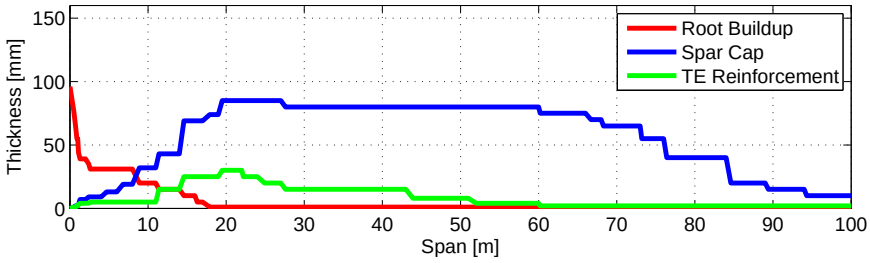

(b) Carbon blade (SNL00-01)

Figure 10: Thickness of the root-build-up, spar cap and trailing edge reinforcement along the blade length for the glass blade.

2. *Carbon blade: SNL00-01*

The glass blade was an initial starting point but was not a cost effective design due to the high blade weight. The development of the glass blade was followed by a series of investigations into the effect of carbon fiber on the blade weight.[17–19] The use of carbon fiber in the design allowed the blade mass to be reduced to 74,000 kg, a decrease of 35%. The blade section is shown in Figure 9b. The blade features carbon fiber in the spar caps; the increased Young's modulus of carbon fiber results in a reduced spar cap thickness. The reduced thickness of the laminate created buckling issues, so the width of the spar cap was reduced. The trailing edge reinforcement was also reduced by 50% in width and the root build-up was thinned. The thickness of the root-build-up, spar cap and trailing edge reinforcement are shown in Figure 10b. More details of the design iterations which led to the *SNL00-01*, as well as the final design, are provided in the above references. The blade design is summarized in the scorecard.[23] As with the glass blade, an opportunity to optimist the carbon blade design to make further mass reductions still exists.

B. Blade Model

The 100 m blade models are read using the SNL computer-aided engineering tool, NuMAD, which was created in MATLAB.[24] NuMAD (Numerical Manufacturing And Design Tool) is used to generate three-dimensional finite element models. However, it was necessary to modify the NuMAD input to generate a blade model in MATLAB to allow the structural efficiency to be evaluated. The external geometry of the blade, shown in Figure 11, was defined from the NuMAD input. The blue lines show the aerofoil stations where there is a

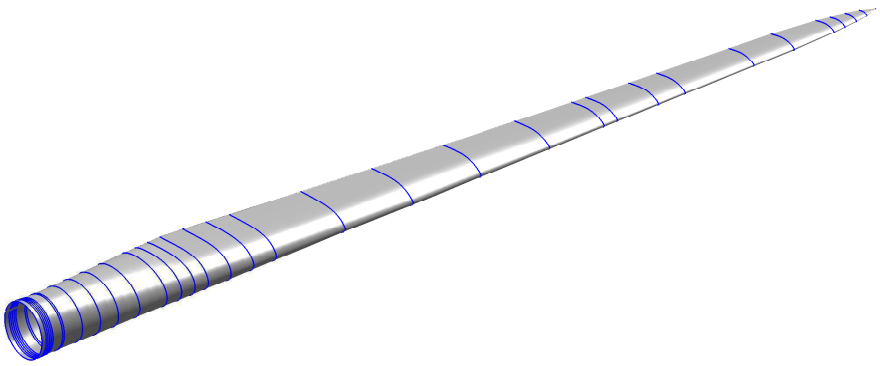

Figure 11: External geometry of the SNL 100 m blade. The blue lines indicate the positions at which the layup or structural layout change.

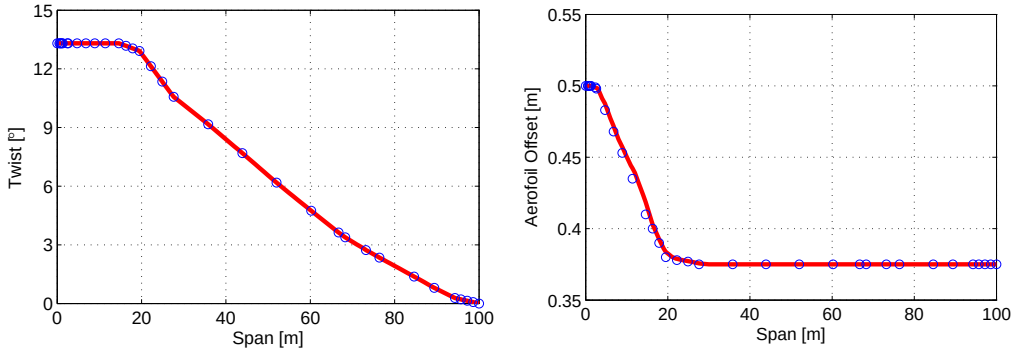

(a) Twist

(b) Aerofoil offset

Figure 12: Data used to generate additional aerofoil stations. The blue data points are from the original NuMAD input and the red line shows the new data.

change in composite layup or structural layout. The NuMAD input consisted of 34 aerofoil stations along the blade length with a concentration at the root. Additional aerofoil stations were added to the blade model in one meter increments, which allowed the structural efficiency to be analyses in regular intervals along the entire length, as opposed to the non-uniformly distributed stations seen in Figure 11. This set-up provided a better resolution of the variation in structural properties along the blade length. The geometry of the new stations were found by interpolating the aerofoil nodes between the original aerofoil stations. It was also necessary to interpolate the twist and aerofoil offset, which are shown in Figure 12.

The internal features, such as the spar caps and webs, were also defined from the NuMAD input. Each of the aerofoil stations was discretised into elemental areas and the rule of mixtures was used to find material properties for each element. An equivalent Young's modulus and thickness for each element was then determined using the rule of mixtures. Next, the section properties of the cross-sections were determined, which allowed the structural efficiency analysis to be performed. Two investigations are conducted for the SNL 100 m blade. The first compares the glass and carbon blade designs while the second evaluates the effect of applying an offset to the spar caps.

IV. Glass vs. Carbon

A comparison of the glass and carbon blades is now presented. The structural efficiency of the bending response is considered, as the blade is slender and is assumed to undergo flexure with no shear deformation.[25]

A. Shape Factors

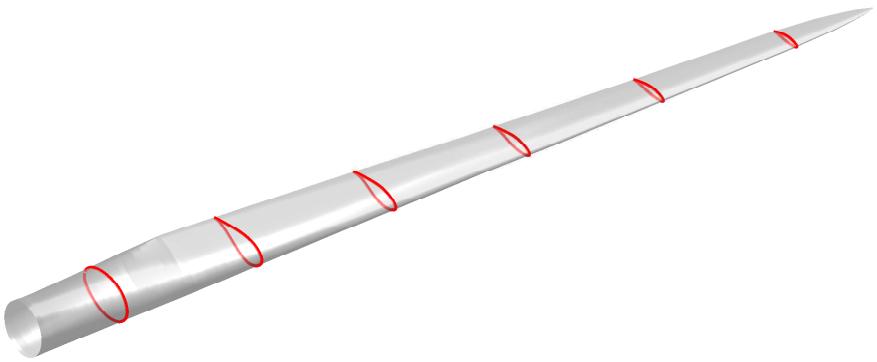

Figure 13: Spanwise positions where the structural efficiency result is presented. Positions are at 10, 30, 50, 70 and 90 m.

It may seem obvious that the carbon blade outperforms the glass blade. However, the shape factors do not account for the effect of the material. The designs may be referred to as the glass and carbon blades, but it is important to remember that, in this section, only the effect of shape, and not material, is accounted for. The results are presented at six stations along the blade, from root to tip. These stations are at spanwise positions of 10, 26, 42, 58, 74 and 90 m, as shown in Figure 13. Bending out-of-plane, in the z-direction, is referred to as flapwise bending, while in-plane bending, in the y-direction, is referred to as edgewise bending. Therefore, the flapwise bending moment is M_y and edgewise bending moment is M_z. A description of the loads is given in Table 1 and the coordinate system for bending is shown in Figure 14. The load angle α is defined to be zero for a positive flapwise moment. The low pressure surface of the aerofoil is in the positive z-direction and the trailing edge is in the positive y-direction. The load cases that are the most important for wind turbine blade design are positive flapwise bending and combined positive flapwise-edgewise bending. Nonetheless, edgewise moments are becoming increasingly significant as the blade size increases. More details of the load cases for the 100 m blade are found in the blade report.[14]

Table 1: Description of loads acting on the wind turbine blade.

α	Description	Moment
0°	Forward Flapwise (out-of-plane)	$+M_y$
90°	Forward Edgewise (in-plane)	$+M_z$
180°	Reverse Flapwise (out-of-plane)	$-M_y$
270°	Reverse Edgewise (in-plane)	$-M_z$

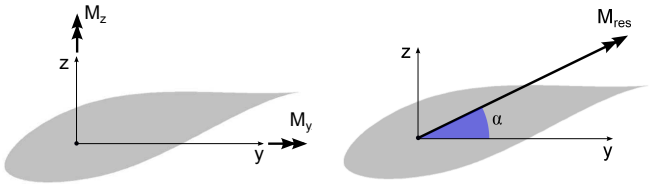

(a) Bi-axial moments. (b) Resultant moment.

Figure 14: Loading on the blade.

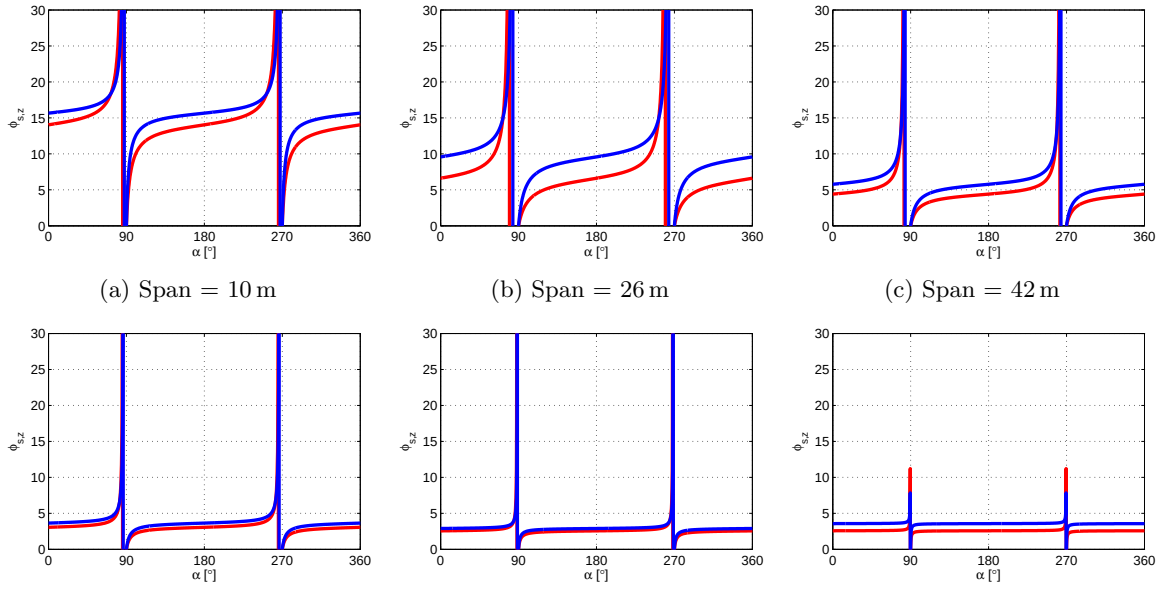

(a) Span = 10 m (b) Span = 26 m (c) Span = 42 m

(d) Span = 58 m (e) Span = 74 m (f) Span = 90 m

Figure 15: Glass/Carbon: z-stiffness shape factor. The red line is the glass blade and the blue line is the carbon blade

1. *Stiffness*

The z-direction (flapwise) stiffness shape factors for the glass and carbon blades are shown in Figure 15. The glass blade is represented by the red line and the carbon by the blue line. The result is shown for the six radial positions detailed in the previous section, from the root to tip. Immediately, it is noted that the results for both blades are similar. The reason for the similarities is that the shape of the sections are closely related. The discrepancies that are observed result from the differences between the positions of the webs and the laminate thickness. The carbon blade has thinner spar caps because carbon fiber is a stiffer material. Thin-walled structures are generally more efficient, so this is the reason for the improvements over the glass blade. At load angles which approach pure edgewise loads ($\alpha = 90°$ and $\alpha = 270°$), the glass blade has slightly higher shape factor values. This is due to the greater distance between the main webs and the larger trailing edge reinforcement. These features contribute to increased stiffness in the y-direction, which results in reduced deflection in the z-direction through bend-bend coupling.

Towards the tip, the shape factors tend to decrease in magnitude as a result of the changes in geometry along the blade. Near the root, the section transitions from a circular section to a thick aerofoil, after which the relative thickness of the aerofoil decreases along the length. The design space is thus more limited towards the tip and the spar caps' contribution to the out-of-plane stiffness is diminished. There is also an effect from the angle of twist of the aerofoil, which is initially high and eventually reduces to zero at the tip (Figure 12a). This trend alters the asymmetric bending response, as changes in the section properties cause the principal angle of the second moment of area to rotate. This effect is seen by observation of the shape of the tangent curve. When the principal angle of the second moment of area is rotated away from the y-axis (at high twist angles), there is more variation in the shape factor from the mean value. This effect reduces along the blade length as a result of the increasing asymmetry of the beam section.

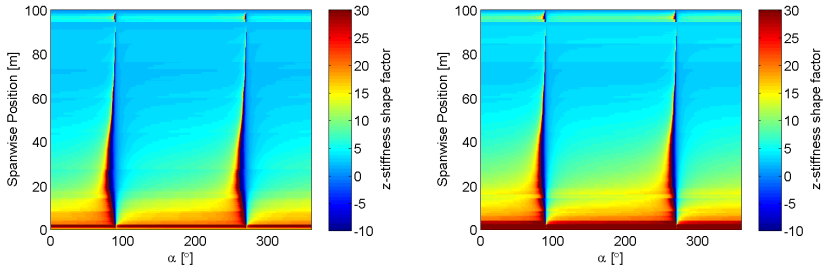

(a) Glass (b) Carbon

Figure 16: Shape factor map for z-direction stiffness.

It is possible to evaluate the shape factor at all positions along the blade for any load angle. Therefore, a structural efficiency map can be created to display the entire performance of the blade. Such maps for the glass and carbon blades are shown in Figure 16. The maps show angle of load α against spanwise position, with the color indicating the shape factor magnitude. The maps have not been interpolated and each square represents the shape factor at that spanwise position and load angle. In the plots, step changes in the spanwise direction are observed. These discontinuities in the structural efficiency occur at the points where the layup changes. In reality, the laminates in a blade are gradually tapered with more ply drops, but this level of detail is not included in the model. The maps show the same trends already observed, with high shape factor magnitudes in the root region and gradually decreasing towards the tip. The exception is close to the tip, where the magnitude of the shape factor increases due to the spar caps and webs ending, leaving only a structural shell. A thin-walled structure is adequate for the lightly loaded tip.

The similarities of the side-by-side maps make it difficult to identify the differences. To address this issue, another map is created that compares the results directly. Figure 17 shows the percentage difference in the z-stiffness shape factor of the carbon blade with respect to the glass blade. Thus, a value of 10% on the map indicates the carbon blade has a 10% higher shape factor than the glass blade. The comparison show that the carbon blade almost always outperforms the glass blade in terms of the shape factor. The improvements in the carbon blade are most notable at the root, near the maximum chord, and at the tip.

The general stiffness shape factor results are also presented as polar plots in Figure 18. For flapwise bending, the carbon blade has larger shape factors than the glass blade. In contrast, the shape factor of

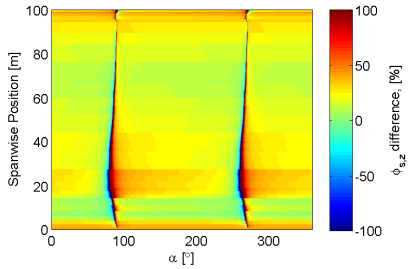

Figure 17: Percentage difference z-direction stiffness shape factor of the carbon blade compared to the glass blade.

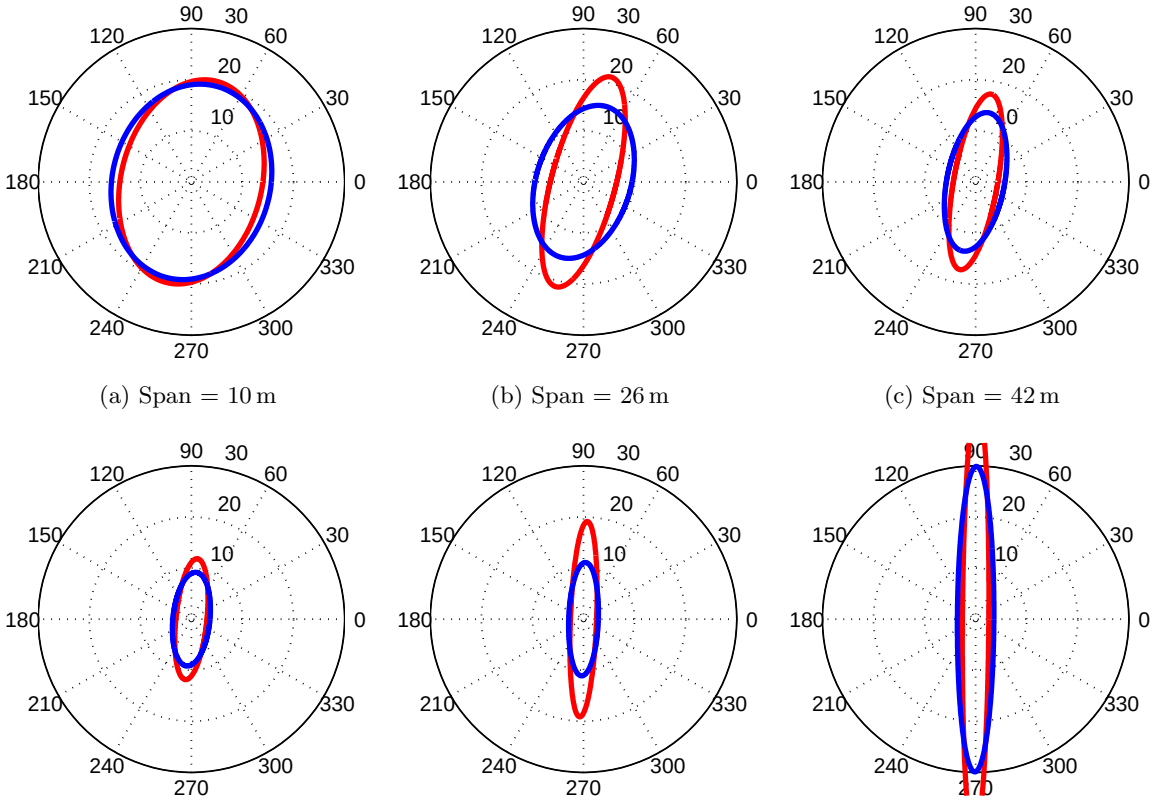

(a) Span = 10 m (b) Span = 26 m (c) Span = 42 m

(d) Span = 58 m (e) Span = 74 m (f) Span = 90 m

Figure 18: Glass/Carbon: General stiffness shape factor. The red line is the glass blade and the blue line is the carbon blade

the glass blade improves for edgewise bending. Previously, the improvement in shape factor for the glass blade arose because of bending coupling. In this case, the improvement is also due to the improved stiffness in the y-direction, as the general stiffness shape factor accounts for the resultant deflection as opposed to a specific direction. Near the root, the shape factors are similar to an axisymmetric section, as the shape is more circular in nature. As the relative thickness of the aerofoil decreases along the length, the shape factor becomes more asymmetric with a dominant direction.

The dominant direction of the shape factor occurs at edgewise load angles due to the nature of the aerofoil geometry, which becomes slender towards the tip. In addition, the twist of the aerofoil is greater nearer the root; therefore, the orientation of the maximum magnitude of the shape factor is offset from the direction of edgewise bending. This angle is related to the principal angle of the second moment of area. At the final section, when the internal features that resit flapwise bending terminate, both shape factors have increased magnitudes for the edgewise bending loads.

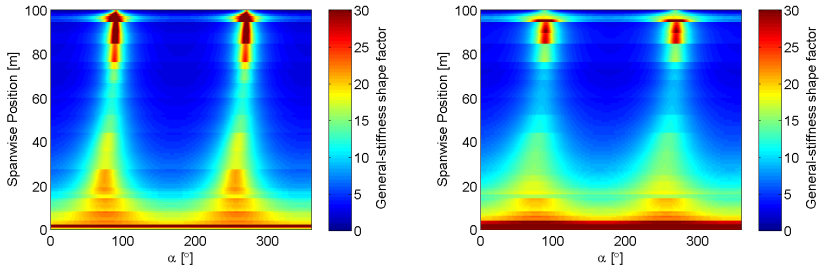

(a) Glass (b) Carbon

Figure 19: Shape factor map for general stiffness.

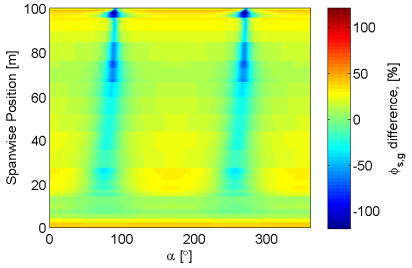

Figure 20: Percentage difference general stiffness shape factor of the carbon blade compared to the glass blade.

The shape factor maps for general stiffness are shown in Figure 19. The maps clearly indicate the trend of higher shape factors for the edgewise dominated load cases. Both maps show a large peak in the shape factor for edgewise loads at the tip. This peak is larger in the glass blade, which is due to the thicker and wider trailing edge reinforcement. For flapwise bending, the carbon blade has an improved performance over the glass blade. The differences are seen more clearly in the comparison map in Figure 20. The carbon blade has lower shape factor magnitudes for a narrow load angle range that is centered around an edgewise load case. It should be reiterated that it is the flapwise bending stiffness which is significant due to higher load magnitudes and required tower clearance. For all the other load angles, the carbon blade is consistently either close to, or outperforming, the glass blade.

2. Strain

The strain shape factor polar plots are shown in Figure 21. Across all the sections, the carbon blade has an improved performance for flapwise loads but decreased performance for edgewise loads. The difference between the shape factors for edgewise loads decreases along the blade length. However, the advantage of the carbon blade remains for flapwise dominated loading. As before, the reason for the large shape factors

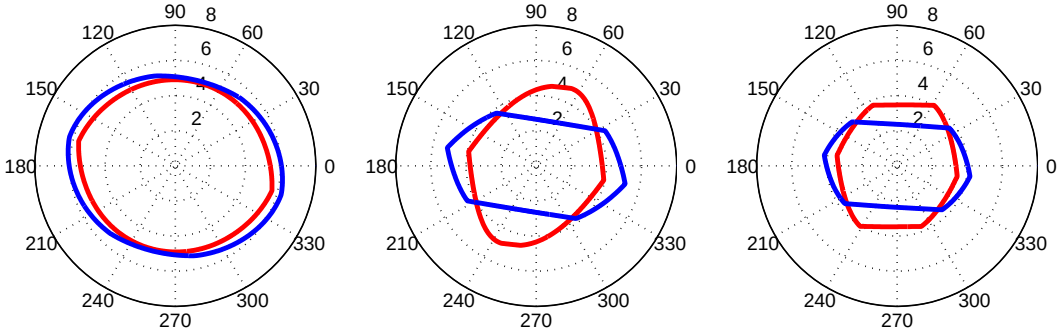

(a) Span = 10 m (b) Span = 26 m (c) Span = 42 m

(d) Span = 58 m (e) Span = 74 m (f) Span = 90 m

Figure 21: Glass/Carbon: Strain failure shape factor. The red line is the glass blade and the blue line is the carbon blade.

in the glass blade for edgewise loads is that it has more trailing edge reinforcement and the shear webs are more widely spaced apart.

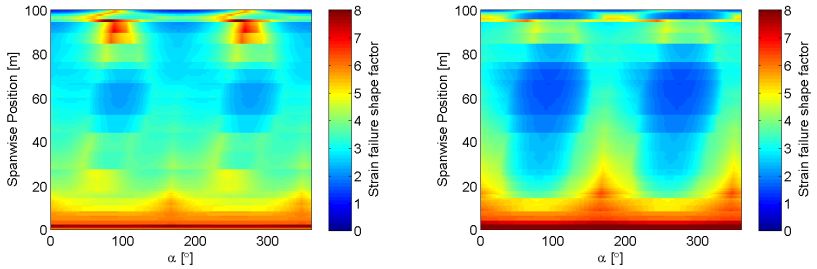

(a) Glass (b) Carbon

Figure 22: Strain shape factor map

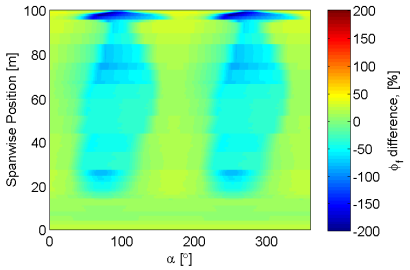

Figure 23: Percentage difference strain shape factor of the carbon blade compared to the glass blade.

The strain shape factor maps for the two blades are shown in Figure 22. Both blades have high shape factor magnitudes near the root, but then drop by as much as 50% in just 10 m. The carbon blade generally shows higher shape factors for flapwise dominated loads, and lower for edgewise dominated loads. Near the blade tip, the shape factor experiences rapid changes that are the result of the webs and spar caps terminating. The response is complicated, although the tip is relatively lightly loaded in terms of bending moments. The comparison plot for the strain shape factor is shown in Figure 23. It clearly indicates the advantage the carbon blade has for flapwise loads and the disadvantage for edgewise loads. The sudden change in the shape factor as it transitions from flapwise to edgewise dominated loads is important when considering combined load cases. During this transition, the beam response is sensitive to small increases in edgewise loads. This finding is particularly significant for wind turbines that are increasing in size.

B. Performance Index

The glass and carbon blades have now been compared in terms of their shape alone. However, the key design difference between the two was the use of carbon fiber. Now the performance index is assessed and the advantages of the carbon blade become clearer.

1. Stiffness

Figure 24 shows the z-direction stiffness performance index. As the superior material properties of carbon fiber are being accounted for, the performance of the carbon blade is approximately 50% higher than for the glass blade. The increases in performance for the carbon blade are only significant beyond the root region because the carbon fiber begins after this point. As with the shape factor, the trend along the blade is an overall reduction in the performance index magnitudes.

The z-direction performance index maps show distinct differences between the blades (Figure 25). The most obvious difference between the two is that the magnitudes of the carbon blade performance index are much higher than in the glass blade, as was seen in the section polar plots. While there are small differences

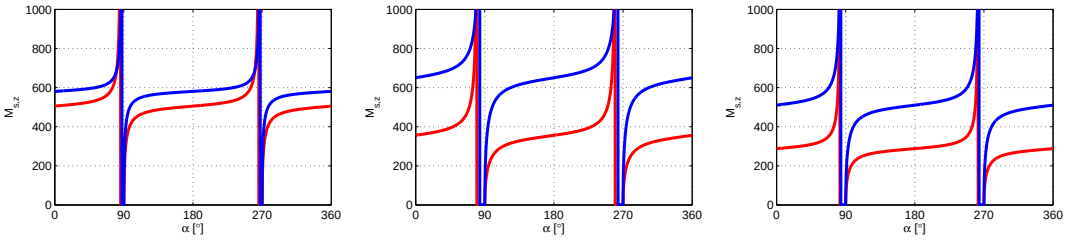

(a) Span = 10 m (b) Span = 26 m (c) Span = 42 m

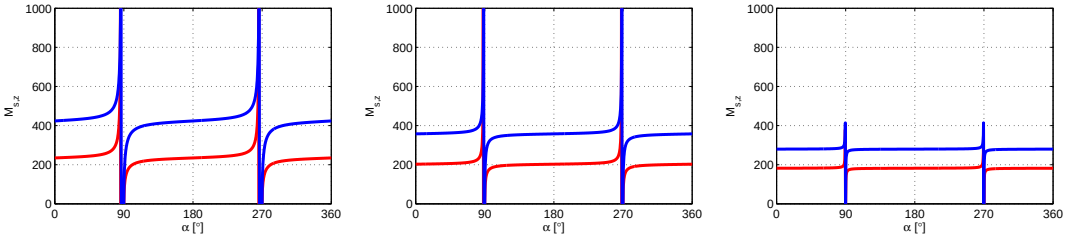

(d) Span = 58 m (e) Span = 74 m (f) Span = 90 m

Figure 24: Glass/Carbon: z-stiffness performance index. The red line is the glass blade and the blue line is the carbon blade.

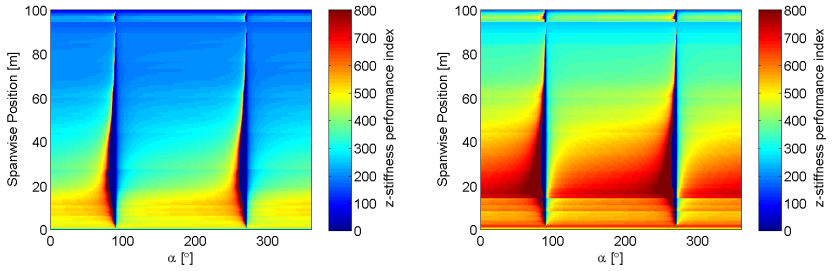

(a) Glass (b) Carbon

Figure 25: z-direction stiffness shape factor map.

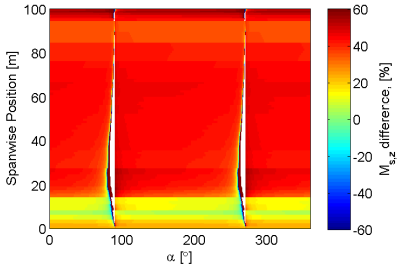

Figure 26: Percentage difference z-direction stiffness shape factor of the carbon blade compared to the glass blade.

in the positions of the peaks and troughs of the map, this effect is relatively insignificant. One of these observations shows a peak in performance index along the radius which occurs at approximately 20 m in the glass blade but at 30 m in the carbon blade. This anomaly may have to do with the reduced thickness in the root build-up of the carbon blade and the relative thickness of the spar caps and trailing edge reinforcement. The comparison map (Figure 26) shows that the carbon blade has a relatively constant improvement beyond the root region. The differences for edgewise bending occur over a small load angle range and are not significant.

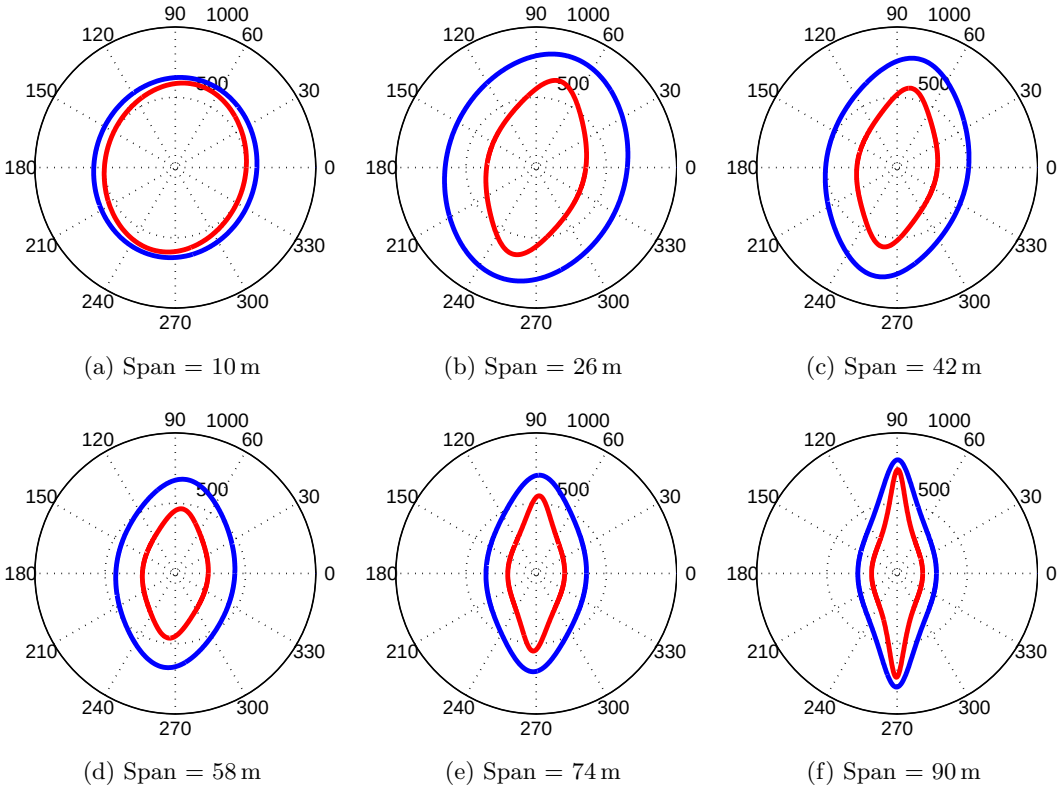

(a) Span = 10 m (b) Span = 26 m (c) Span = 42 m

(d) Span = 58 m (e) Span = 74 m (f) Span = 90 m

Figure 27: Glass/Carbon: General stiffness performance index. The red line is the glass blade and the blue line is the carbon blade.

The polar plots for the general stiffness performance index are given in Figure 27. The most notable difference between the shape factor and performance index of the z-direction stiffness was the difference in relative magnitudes. With regards to the general stiffness, the magnitude of the carbon blade values are significantly higher and the shape of the polar plots is different. Instead of the oval shape of the shape factor, the performance index has a 'pinched' appearance. The shape is a result of the square root applied to the shape factor in the performance index formulation. This effect also occurs in the z-stiffness shape factor but is seen more prominently in the performance index polar plot compared to the ovals of the shape factor. The pinched shape becomes more prominent when the difference between the major and minor principal axes is larger (when γ is higher).

Figure 28 shows the general stiffness performance index maps. The key difference is the consistently higher magnitudes in the carbon blade. The discrete jump in magnitude of performance index is again seen in the carbon blade, at the point where the carbon fiber spar cap begins. The comparison between the two designs (Figure 29) shows the same trends as the z-direction stiffness shape factor. The main change is that the difference between the shape factors reduces slightly for edgewise bending load angles, the result of increased distance between the webs and increased trailing edge reinforcement.

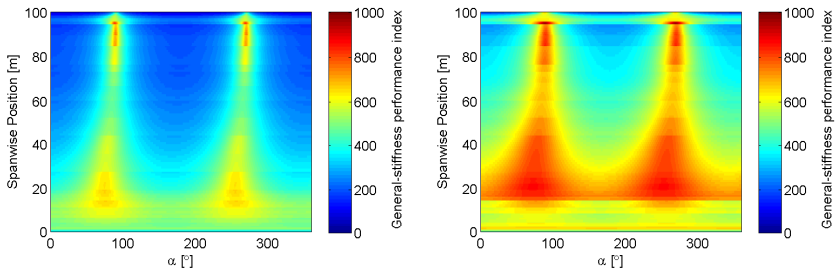

(a) Glass (b) Carbon

Figure 28: General stiffness performance index map.

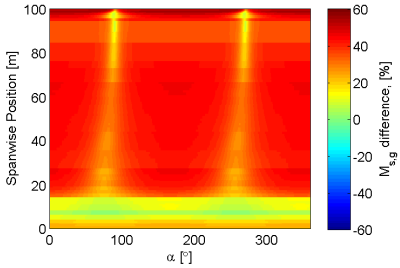

Figure 29: Percentage difference general stiffness performance index of the carbon blade compared to the glass blade.

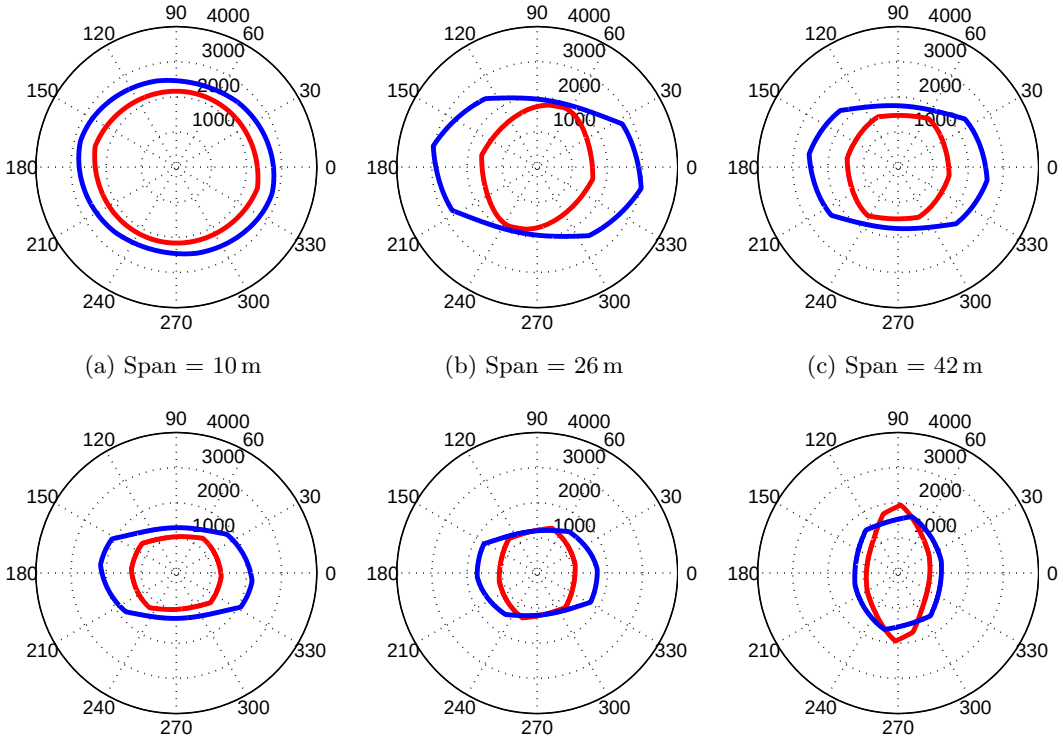

(a) Span = 10 m (b) Span = 26 m (c) Span = 42 m

(d) Span = 58 m (e) Span = 74 m (f) Span = 90 m

Figure 30: Glass/Carbon: Strain performance index. The red line is the glass blade and the blue line is the carbon blade.

2. Strain

As with the z-direction stiffness, the structural advantage of the carbon blade is clearly seen in strain performance index polar plots (Figure 30). The carbon blade has higher performance indices for all values of α, with the exception being at the tip. The biggest advantage is seen for flapwise dominated loads. Conversely, the advantage for edgewise dominated loading is more marginal at inboard sections. Aside from the difference in magnitude, there is a general rotation of the polar plots moving from the root to the tip. In other words, the maximum values of the performance indices rotate in a positive angular direction. The glass blade tends to have less variation in magnitude of performance index with changing load direction.

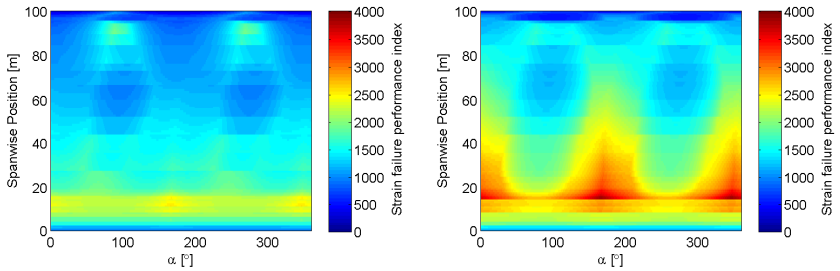

(a) Glass (b) Carbon

Figure 31: Strain performance index map.

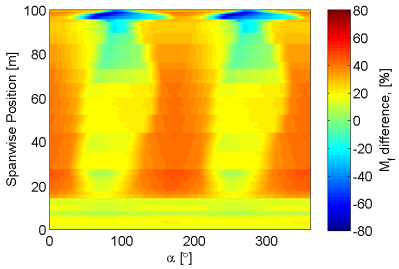

Figure 32: Percentage difference strain performance index of the glass blade compared to the carbon blade.

The strain failure performance index maps are shown in Figure 32. Again, the most significant difference between the glass and carbon blades is the magnitude of the performance index, as opposed to the relative positions of the map. The carbon blade has a greater range of performance index that is generally better for flapwise loads and lower for edgewise loads. The glass blade also shows this trend but with lower magnitudes and over a smaller range. The comparison map (Figure 32) shows the advantage the carbon blade has over the glass blade. The carbon blade outperforms the glass blade for all load angles at all spanwise positions, except the tip. The improvement over the glass blade is seen in a load range that centers around pure flapwise loading ($\alpha = 0°$ and $\alpha = 180°$). Therefore, the carbon blade has significant performance gains but, once the load exceeds $\alpha \approx 50°$, the advantage is diminished.

To allow further understanding of the strain performance index result, another map has been created that shows the variation in neutral axis (Figure 33). The plots show the difference between the neutral axis angle and the load angle. At the root, both blades show little or no difference between the neutral axis and the load angle, as expected for an approximately circular section. Towards the tip, the relative thickness of the aerofoil reduces, and the section becomes more asymmetric. Therefore, the difference between the load direction and neutral axis increases. Also demonstrated are abrupt changes in the neutral axis with small changes in the load direction. The performance of the carbon blade is clearly superior to the glass blade, although the performance index was based on a mass objective and did not account for cost.

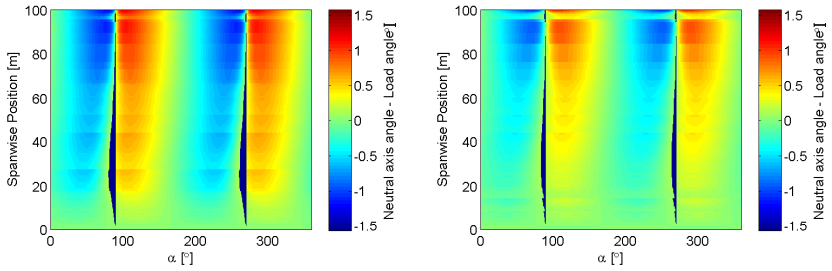

(a) Glass (b) Carbon

Figure 33: Angle between neutral axis and applied load angle.

C. Summary

The carbon blade was found to perform slightly better than the glass blade in terms of the shape factors, particularly for flapwise bending. The differences were driven by the positions of the shear webs and the thickness of the laminates in the spar caps and trailing edge reinforcement. The shape factors for the carbon blade were better than the glass blade, but the real benefits were seen when considering the performance index. Beyond the root region, the magnitudes of the stiffness performance indices were consistently higher for all load angles. For the strain performance index, the values were almost always higher, particularly for flapwise loads. A wind turbine blade design considers the trade-off between the cost and mass. However, because of the complexity involved in wind energy costs where this balance lies is not obvious. The glass blade has a high mass, which would not be cost-effective in a real wind turbine. Equally unlikely would be a blade made entirely of carbon fiber. The first approach is high mass and low cost, while the second is the inverse. In reality, the real solution is a compromise between these approaches.

V. Offset Spar Caps

Studying the structural efficiency of the carbon and glass blades was a comparison between two existing designs. This comparison allows a better understanding of a successful design or can be used for concept selection. It is also possible for analysis of the structural efficiency to be fed back into the design process. In this section, the structural efficiency analysis is used to investigate the effect of such a design change. Using the standard carbon blade (*SNL00-01*) as a starting point, the position of the spar caps is altered. This design change is based on the result of topology optimization from a previous study which showed a topology that featured offset spar caps.[9] The nature of the topology optimization means that the results are less well developed, whereas now the structural efficiency is applied to a much more refined blade design. Instead of recreating the exact result from the topology optimization, an offset is applied to the spar caps to determine what effect this single change has on the structural efficiency.

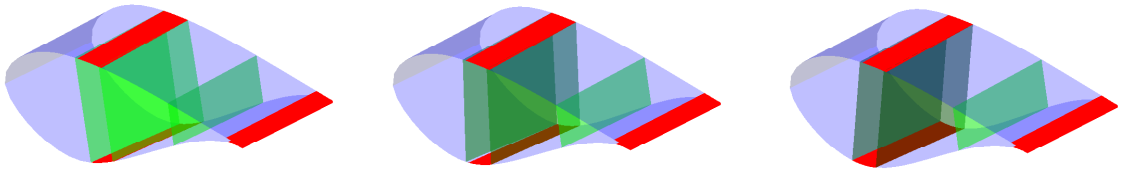

(a) 0% offset (b) 5% offset (c) 10% offset

Figure 34: Spar cap offset. The high pressure spar cap is moved towards to leading edge by a given percentage of the chord.

A simple offset was applied to the carbon blade by moving the high pressure spar cap towards the leading edge by a given percentage of the chord. Offsets of 5% and 10% of the chord were applied, with the new

geometry shown in Figure 34. The 0% offset design is the original *SNL00-01* design. The reduction in the relative thickness of the aerofoil along the blade length means the angle of the offset increases towards the tip. The dependence of the angle of the spar cap offset on the length matches the results of the topology optimization, which had an increasing offset angle along the blade length. The reason for moving only the high pressure spar cap is that in the original design, both spar caps are already positioned slightly aft of the maximum thickness of the aerofoil. Applying a design change, such as the spar cap offset, is a simple design modification that demonstrates how a small design modification affects the structural efficiency.

In the comparison between the glass and carbon blades, the shape factor and performance index results were both presented, to demonstrate the contribution that shape made to the structural efficiency. For the comparison between the offset designs, the trends that are observed in the shape factors are also observed in the performance index results. This is because the differences are driven by the position of the spar caps, as opposed to the material selection (which was significant when comparing the glass and carbon blades). For this reason, the shape factor results are not presented in the main text.

A. Performance Index

1. Stiffness

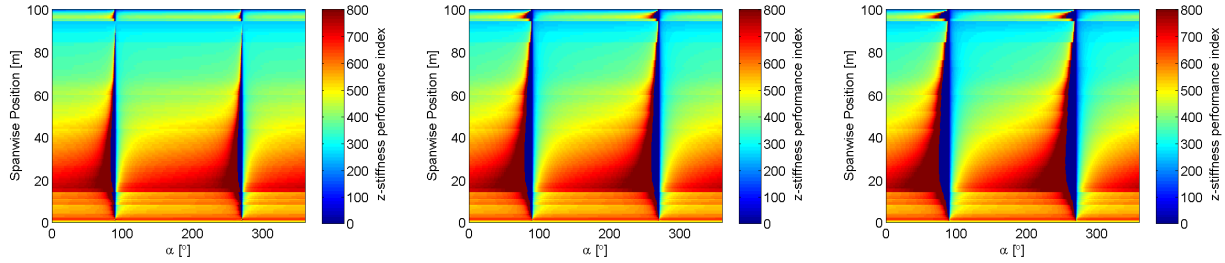

(a) 0% Offset (b) 5% Offset (c) 10% Offset

Figure 35: z-direction stiffness performance index map.

The differences between the blades are subtle but, in general, a larger offset provides an improvement for the key load cases (positive M_y and M_z, or $0° < \alpha < 90°$). The mean value of the tan curve appears to remain the same for the sections but the asymmetry changes with increasing offset. This characteristic is related to the rotation of the principal angle of the second moment of area, which results in a greater misalignment with the y-axis. It is important to note that, although there is an improvement for the combined load cases, the performance for pure edgewise loading is unaffected. The z-direction stiffness performance index maps are shown in Figure 35. The plots are closely related, with similar magnitudes. The main difference is that from approximately $0° < \alpha < 90°$ and $180° < \alpha < 270°$, a trend for the higher offset section to have higher magnitudes of performance index is noted. Conversely, the performance is decreased for $90° < \alpha < 180°$ and $270° < \alpha < 360°$, but these load angles are less critical. Most importantly, the structural efficiency for pure edgewise bending does not decrease, while the critical load directions have a slight advantage.

The comparison for the z-direction stiffness shape factors is shown in Figure 36. The comparison are made for the 5% and 10% offset blade with respect to the 0% offset blade (the *SNL00-01* carbon blade). Therefore, a negative difference indicates that the offset blade performed better than the original blade. The differences are most significant near $\alpha = 90°$ and $\alpha = 270°$ (edgewise bending loads). While these load cases are less critical, the large increases at these load cases also result in increases in the shape factor for flapwise loads. The increase is due to a beneficial bend-bend coupling between edgewise loading and flapwise deflection.

In general, the effect of increasing the offset is a rotation of the maximum shape factor towards the direction of flapwise loading. The general stiffness performance index maps are given in Figure 37. The plots indicate an increase in the maximum magnitude of performance index, as well as a corresponding decrease in the minimum magnitude. It appears that improvement for the important loading conditions comes at the expense of reduced structural efficiency for the less important load angles. As the twist along the length of the blade reduces, there is a general trend for the maximum value of the shape factor to occur at pure

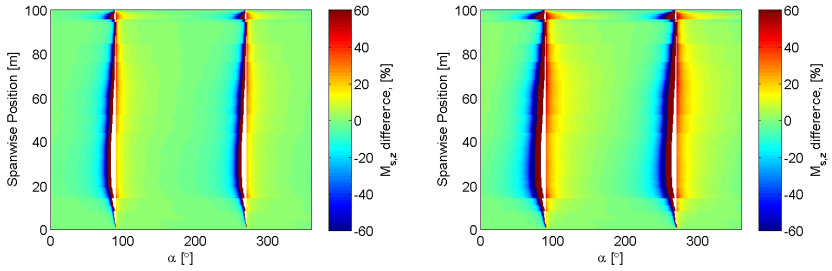

(a) 5% Offset (b) 10% Offset

Figure 36: Percentage difference z-direction stiffness performance index of the offset blades, relative to the carbon blade.

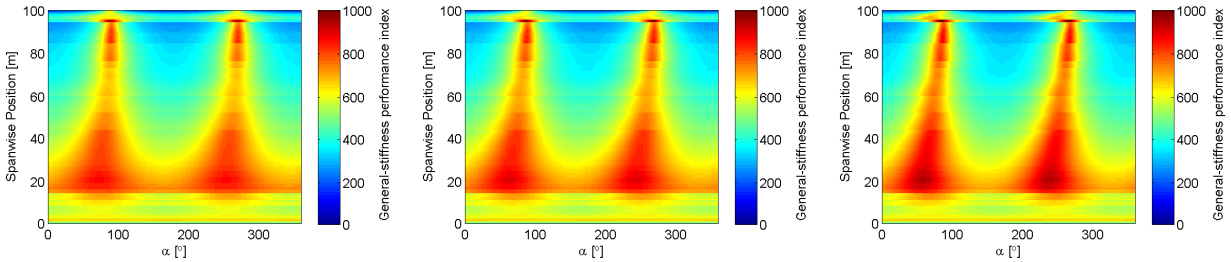

(a) 0% Offset (b) 5% Offset (c) 10% Offset

Figure 37: General stiffness performance index map.

edgewise load angles. The relative difference in principal angle between the offset sections remains constant.

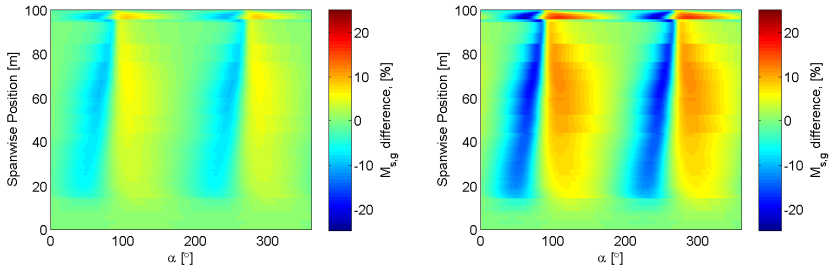

(a) 5% Offset (b) 10% Offset

Figure 38: Percentage difference general stiffness performance index of the offset blades, relative to the carbon blade.

The comparison plots for the general stiffness shape factor are shown in Figure 38. Compared to the z-direction stiffness, the general stiffness shape factor shows differences over a wider range of load angles because the offset also affects the stiffness in the y-direction through bending coupling. The increasing offset offers significant increases in the performance index for certain load angle ranges. However, there are corresponding decreases in performance index for other load angle ranges. The transition between improvements and decreases in performance occurs with small changes in load angle, near $\alpha = 90°$ and $\alpha = 270°$. It appears that the offset spar caps improve the stiffness performance for certain load cases, but at the expense of a reduction for other load cases (which are less significant in terms of acting as design drivers).

2. Strain

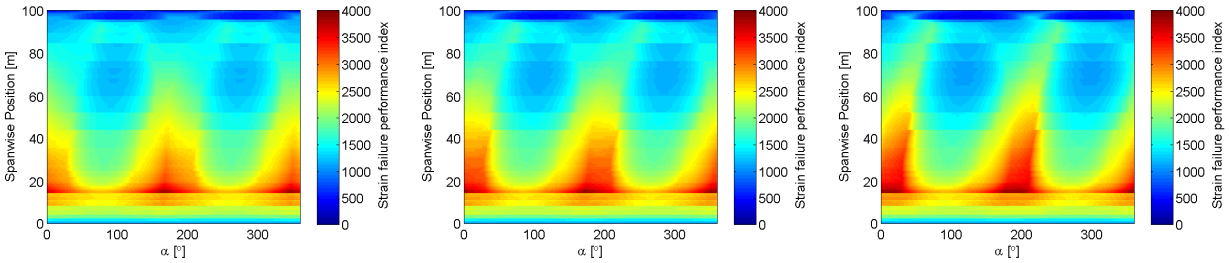

(a) 0% Offset (b) 5% Offset (c) 10% Offset

Figure 39: Strain performance index map

The strain performance results show more variation when compared to the stiffness performance results (Figure 39). As the offset increases, the performance index is higher for $0° < \alpha < 120°$ and $180° < \alpha < 270°$. The advantage at these load angles is greater than the reduction at the remaining load angles. Significant differences in both the magnitudes and the positions of the peak values for the different offsets are observed. As the offset increases, the peak value of the performance index increases for flapwise dominated loading, most notably at a spanwise position of 20 m. Overall, the higher offset has higher magnitudes of performance index. Moving towards the tip of the blade, the position of the peak magnitude occurs at increasing values of α.

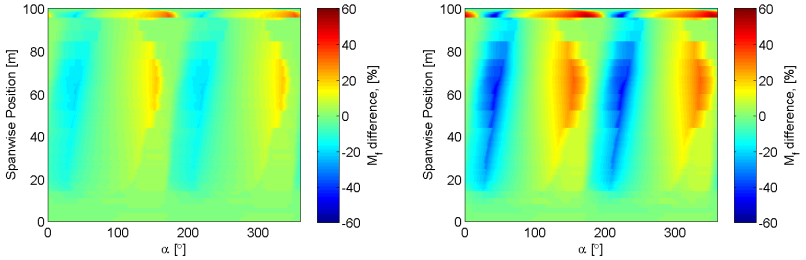

(a) 5% Offset (b) 10% Offset

Figure 40: Percentage difference strain performance index of the offset blades, relative to the carbon blade.

The comparison between the strain performance indices (Figure 40) demonstrates the load angles at which the offset spar cap provides the greatest benefits. The biggest improvements are at load angles near $\alpha = 45°$, compared to the stiffness performance index where the benefits were for higher values of α. Along the blade span, the benefit of the offset generally improves for the crucial load angles. In the topology optimization results, the spar caps gradually become more offset along the blade length. This result shows that the offset spar caps also have an increasing benefit along the blade length.

B. Summary

The general conclusion is that applying an offset can improve the structural efficiency, but only for certain load angles. These improvements occurred at the critical load angles. Although the results showed improvements for the stiffness, the main benefit was for the strain performance index. Applying the spar cap offset is an example of a simple design modification. However, more advanced design modifications can be applied to the design. Such design changes might include translating the positions of both spar caps and varying the offset along the blade length. Other features such as trailing edge reinforcement could also be incorporated. The design could have trailing edge reinforcement in the first half of the blade, then transition to an offset spar cap design. The low computation cost of the structural efficiency analysis means that numerous design modifications can be made in small increments. It is then possible to animate the results of the gradual

changes in the structural efficiency map to allow observation of the effect of the design changes. Thus, the effect of design modifications could be visualized easily.

VI. Conclusion

The shape factors at specific sections give detailed views of the shape factors and the maps provide an impression of how the structural efficiency evolves along the blade length. Evaluating the structural efficiency of a wind turbine blade, which is a complex structure composed of numerous material, was necessary. The size of wind turbines are continuing to increase. Clearly, a 15 m blade is completely different from a 100 m blade, yet the basic structural design has not evolved significantly.

The addition of carbon fiber to a wind turbine blade results in a lighter design (although cost increases). However, the blade is not simply lighter with the same bending response; the behavior changes. The comparison between the glass and carbon blades showed that there were differences in the structural efficiency that resulted from both the shape and the material choice. In terms of shape alone, the performance of the carbon blade was improved for flapwise loads, compared to edgewise. When the performance index is considered, the carbon blade is still superior in edgewise bending, in addition to flapwise bending. The higher stiffness carbon fiber spar cap required a reduced distance between the shear webs and reduced trailing edge reinforcement. The asymmetry of the blade was consequently altered and, thus, resulted in different bending behavior. The comparison shows that the use of carbon fiber does not simply result in having the same bending behavior for reduced weight. With a deeper understanding of the resulting behavior, beneficial effects can be exploited. Taking advantage of such a positive effect was demonstrated with the offset spar caps. The structural efficiency maps show a complete picture of the bending behavior and indicate relative strengths and weaknesses. The offset spar caps aligned more closely with a load case which would represent a combination of in-plane and out-of-plane bending. The comparison shows that with a simple offset applied to the spar caps, the structural efficiency of the blade can be improved for the critical load directions. The improvements in the offset design could be seen to outweigh the decreases in performance, which occur for less important load directions.

The comparison of blade designs show how the structural efficiency analysis methods used in this study can be a useful tool to evaluate different concepts. The analysis can be used to identify potential weak points and predict how the blade might behave at any load case without having to run an individual analysis each time. Future work could include extending the performance index to allow for a cost objective as opposed to simply mass. This would allow the economic advantages of glass to be taken into account. A more advanced design modification could be made to the carbon blade, for example with changes in the size of trailing edge reinforcement and a variable spar cap offset.[26] The design could also be evaluated in finite element analysis to give a more detailed assessment of the blade performance.

Acknowledgments

The research was supported by the EPSRC, as part of the doctoral training center at the Advanced Composite Centre for Innovation and Science (ACCIS), and Vestas Wind Systems, which is gratefully acknowledged. This study was a collaboration between ACCIS and Sandia National Laboratories as part of an international research placement.

Sandia National Laboratories is a multi-program laboratory managed and operated by Sandia Corporation, a wholly owned subsidiary of Lockheed Martin Corporation, for the U.S. Department of Energy's National Nuclear Security Administration under contract DE-AC04-94AL85000.

References

[1]T. D. Ashwill. Materials and innovation for large blade structures: Research opportunities in wind energy technology. In *50th AIAA Structures, Structural Dynamics, & Materials Conference*, Palm Springs, May 2009.

[2]Ryan Wiser and Mark Bolinger. 2012 wind technologies market report. Technical report, US Department of Energy, August 2013.

[3]F. M. Jensen. *Ultimate strength of a large wind turbine.* PhD thesis, Technical University of Denmark, May 2008.

[4]Paul S Veers, Thomas D Ashwill, Herbert J Sutherland, Daniel L Laird, Donald W Lobitz, Dayton A Griffin, John F Mandell, Walter D Musial, Kevin Jackson, and Michael Zuteck. Trends in the design, manufacture and evaluation of wind turbine blades. *Wind Energy*, 6(3):245–259, 2003.

[5]S. Joncas. *Thermoplastic Composite Wind Turbine Blades; An Integrated Design Approach.* PhD thesis, Technische Universiteit Delft, 2010.

[6]P. M. Weaver and M. F. Ashby. The optimal selection of material and section-shape. *Journal of Engineering Design*, 7(2):129–150, 1996.

[7]M. F. Ashby. Overview no. 92: Materials and shape. *Acta Metallurgica et Materialia*, 39(6):1025 – 1039, 1991.

[8]P. M. Weaver and M. F. Ashby. Material limits for shape efficiency. *Progress in Materials Science*, 41:61–128, 1997.

[9]Neil Buckney, Alberto Pirrera, Steven D. Green, and Paul M. Weaver. Structural efficiency of a wind turbine blade. *Thin-Walled Structures*, 67:144–154, 2013.

[10]M. F. Ashby. *Materials Selection in Mechanical Design*. Elsevier, 3rd edition, 2008.

[11]J. B. Caldwell. Structures and materials: Progress and prospects. *Philosophical Transactions of the Royal Society of London. Series A, Mathematical and Physical Sciences*, 273(1231):61–75, 1972.

[12]J. G. Parkhouse. Damage accumulation in structures. *Reliability engineering*, 17(2):97–109, 1987.

[13]R. W. Birmingham and J. A. D. Wilcox. Charting the links between material selection and elemental form in structural design. *Journal of Engineering Design*, 4(2):127–140, 1993.

[14]D.T. Griffith and T.D. Ashwill. The sandia 100-meter all-glass baseline wind turbine blade: Snl100-00. Technical report, Sandia National Laboratories, June 2011.

[15]D Todd Griffith, Thomas D Ashwill, and Brian R Resor. Large offshore rotor development: Design and analysis of the sandia 100-meter wind turbine blade. In *53rd AIAA Structures, Structural Dynamics, and Materials Conference*, Honolulu, HI, April 2012.

[16]Sandia National Laboratories. Offshore wind: Sandia large rotor development, May 2013.

[17]D. Todd Griffith, Brian R. Resor, and Thomas D. Ashwill. Challenges and opportunities in large offshore rotor development: Sandia 100-meter blade research. In *AWEA WINDPOWER 2012 Conference and Exhibition*, Atlanta, GA, USA, June 2012.

[18]D. Todd Griffith. Large rotor development: Sandia 100-meter blade research. In *Wind Turbine Blade Manufacturer 2012 Conference*, Dusseldorf, Germany, November 2012.

[19]D.T Griffith. The snl100-01 blade: Carbon design studies for the sandia 100-meter blade. Technical report.

[20]HJT Kooijman, C Lindenburg, D Winkelaar, and EL van der Hooft. Dowec 6 mw pre-design. Technical Report DOWEC-F1W2-HJK-01-046/9, Energy Research Center of the Netherlands (ECN), Petten, the Netherlands, September 2003.

[21]Sandia large rotor design scorecard (snl100-00). Technical Report SAND2011-9112P, Sandia National Laboratories, Albuquerque, New Mexico, USA, 2011.

[22]Sandia large rotor design scorecard. Technical report, Sandia National Laboratories, December 2011. SAND2011-9113P.

[23]Sandia large rotor design scorecard (snl100-01). Technical Report SAND2012-10793P, Sandia National Laboratories, Albuquerque, New Mexico, USA, 2012.

[24]Jonathan C. Berg and Brian R. Resor. Numerical manufacturing and design tool (numad v2.0) for wind turbine blades: Users guide. Technical Report SAND2012-7028, Sandia National Laboratories, Albuquerque, New Mexico, USA, August 2012.

[25]A. Amany and D. Pasini. Material and shape selection for stiff beams under non-uniform flexure. *Materials & Design*, 30(4):1110–1117, 2009.

[26]N. Buckney, S. D. Green, A. Pirrera, and P. M. Weaver. On the structural topology of wind turbine blades. *Wind Energy*, 16:545–560, May 2013.